Available online at www.sciencedirect.com
ScienceDirect
Surface Science 601 (2007) 1930–1936
SURFACE SCIENCE
www.elsevier.com/locate/susc

Chiral surfaces and metal/ceramic heteroepitaxy in the Pt/$SrTiO_3$(621) system

Andrew J. Francis [a], A.J. Koritnik [b], Andrew Gellman [b], Paul A. Salvador [a,*]

[a] Department of Materials Science and Engineering, Carnegie Mellon University, Pittsburgh, PA 15213, USA
[b] Department of Chemical Engineering, Carnegie Mellon University, Pittsburgh, PA 15213, USA

Received 17 November 2006; accepted for publication 15 February 2007
Available online 1 March 2007

Abstract

Low-energy electron diffraction (LEED), atomic force microscopy (AFM), and X-ray diffraction (XRD) have been used to investigate the structural and morphological character of a naturally chiral ceramic $SrTiO_3$(621) substrate and of Pt and Cu thin films deposited on its surface. AFM experiments showed that as-received chirally-oriented $SrTiO_3$(621) substrates display atomically smooth surface morphologies, while LEED patterns revealed that the surface structure has a net chirality. Pt(621) and Cu(621) thin films were grown heteroepitaxially on $SrTiO_3$(621) substrates, as confirmed by XRD. AFM showed that the film surfaces were atomically smooth and LEED illustrated that the Pt films exhibit surface chirality, and by implication that the atomically-flat chirally-oriented Cu films also have chiral surfaces. The characteristics of the observed LEED patterns, where splitting of diffraction spots is considered to arise from the kinked step features of naturally chiral fcc metal surfaces, are discussed with respect to existing models. These results indicate that the chiral $SrTiO_3$(621) ceramic surface drives the growth of single-enantiomer, chiral, metal (621) thin films.

Keywords: Low-energy electron diffraction (LEED); Surface structure; Epitaxy; Platinum; Copper; Titanium oxides; High-index single-crystal surfaces

1. Introduction

The ideal surfaces of many high-index crystal planes (rigorously those with Miller indices (*hkl*) $h \neq k \neq l \neq h$ and $h \times k \times l \neq 0$) of fcc metals are characterized by "step–kink–terrace" structures that have a net chirality, although the bulk crystal is highly symmetric and achiral [1–3]. The step, kink, and terrace features in these "naturally chiral" surfaces arise from nanospaced microfacets whose habits correspond to one of the three low-index planes: (100), (110), and (111). The kink represents the point of intersection of the three facets, and it is the asymmetric geometric and crystallographic arrangements of atoms around the kink sites that render the surfaces chiral [2,3]. Single crystal metal surfaces having chiral orientations of this description can be homochiral, as has been shown using low-energy electron diffraction (LEED) experiments [1]. Importantly, such surfaces have also demonstrated enantioselectivity in their interactions with chiral molecules [4,5]. The enantioselective environments provided by such naturally chiral surfaces are of interest for their potential use in chiral separations and reactions, which are currently difficult and costly to carry out in practice.

Since large-area chiral surfaces are necessary for practical purposes, it would be of interest to obtain metal thin films having homochiral surfaces on robust ceramic supports. Unfortunately, little is known about the real surface structure of "chirally-oriented" ceramic crystals whose crystal structures match those of fcc metals closely enough to promote heteroepitaxial, homochiral growth. A "chirally-oriented" crystal is a crystal whose global surface normal is oriented parallel to the normal of a high-index chiral plane. Ideally, a chirally-oriented crystal would expose a

* Corresponding author. Tel.: +1 412 268 2702; fax: +1 412 268 7596.
E-mail address: paul7@andrew.cmu.edu (P.A. Salvador).

0039-6028/$ - see front matter © 2007 Elsevier B.V. All rights reserved.
doi:10.1016/j.susc.2007.02.026

chiral surface, but this may not hold true because real surfaces can undergo atomic rearrangements and faceting. The focus of this report is to demonstrate that chirally-oriented $SrTiO_3$(621) crystals do indeed expose chiral surfaces and that these surfaces can be used as substrates for deposition of fcc metal films having homochiral surfaces. This achievement represents the first step towards the goal of preparing large area ceramic-supported chiral metal surfaces, although less expensive substrate crystals would be preferable in applications.

Pt and Cu crystallize in the fcc structure and are known to exhibit chiral surfaces along high-Miller index directions [5–8]. $SrTiO_3$ is a commercially available single crystal that adopts the cubic perovskite structure, which can be described as an fcc derivative wherein Sr atoms occupy the corner positions, O atoms occupy the face-centered positions, and the Ti occupies the normally vacant octahedral interstice at the body center of the fcc cell [9]. The crystallographic similarities between fcc metals and $SrTiO_3$, including the fact that $SrTiO_3$ has a lattice mismatch of just 0.5% with Pt and 8.0% with Cu (see Ref. [10] or [11]), allow epitaxial growth of Pt and Cu to occur on $SrTiO_3$ [12–20]. In a previous report, we deposited high-index Pt(621) thin films on single-crystal $SrTiO_3$(621) substrates [9], which confirmed that homochirally-oriented Pt thin films could be grown heteroepitaxially on homochirally-oriented $SrTiO_3$ single crystals. Monte Carlo simulations were later used to further understand the films' microstructural development [21]. It was not determined in either case, however, if the films actually had *chiral surfaces*. Additionally, although a significant amount of research has focused on understanding the structure and stability of low index surfaces of $SrTiO_3$ (see Refs. [22–26], for examples), very little is known about the surface structure of high-index terminations.

In the current work, we use low-energy electron diffraction (LEED), a surface-sensitive technique, to probe the surface crystallinity of both the single crystal $SrTiO_3$(621) substrate and a morphologically flat epitaxial Pt(621) thin film. We also present the heteroepitaxial growth of Cu(621) films on $SrTiO_3$(621) and compare the results with those for Pt films. We will discuss the features of the LEED patterns, in particular splitting of diffraction spots, and confirm the existence of both naturally chiral ceramic surfaces ($SrTiO_3$) and chiral fcc metal thin film surfaces (Pt).

2. Experimental

Polished single crystal substrates of (621)-oriented $SrTiO_3$ ($10 \times 10 \times 1$ mm, miscut $<0.5°$) were obtained from Crystal GmbH (Germany). Samples were prepared by first cutting these crystals into $5 \times 3 \times 1$ mm specimens using a diamond-impregnated wire in a paraffin/water lubricant. Directly before use, the samples were ultrasonically cleaned in acetone, followed by ethanol, for 5 min each. Crystals prepared in this manner are called as-received samples.

Pt and Cu thin films were deposited on $SrTiO_3$(621) single crystals using pulsed laser deposition (PLD); full experimental details are found elsewhere [9,11,19,20]. Briefly, as-received $SrTiO_3$(621) substrates were placed into a PLD system and either a Pt or a Cu foil of 0.25 mm thickness was used as the PLD target. Depositions were performed using a laser energy density at the target of ≈ 8.0 J/cm^2, a wavelength of $\lambda = 248$ nm, a frequency of 3 Hz, a target-to-substrate distance of ≈ 60 mm, and a dynamic atmosphere of 1.3 Pa of O_2 (Ar) for Pt (Cu). Films were deposited using a three-step process that produces films that are both morphologically flat and epitaxially (621)-oriented. This procedure was developed originally by Wagner et al. [27], later used to deposit (1 0 0)-oriented Pt and Cu films on $SrTiO_3$(1 0 0) [19], and then applied in the present work. First, a short high temperature deposition, at a substrate temperature of $T = 600$ °C (300 °C) for Pt (Cu), was carried out to deposit epitaxial nanoscale island-like seed grains. Second, a longer low temperature deposition, $T = 250$ °C (100 °C) for Pt (Cu), was carried out to deposit a nanocrystalline layer that was morphologically flat. Third, a 60 min high-temperature anneal, $T = 600$ °C (300 °C) for Pt (Cu), was carried out to allow the seed grains to grow through the matrix grains to produce a flat and epitaxial layer.

Atomic force microscopy (AFM) was used, as described elsewhere [9,11,19,20], to measure the topographic features of both $SrTiO_3$ substrates and Pt and Cu films. Images were recorded using an atomic force microscope fitted with a 5 μm scan head for optimal lateral resolution. Scanning was performed in contact mode using gold-coated sharpened microlever tips. The AFM was operated at scan rate = 2 Hz, force = 1.5 pN, and gain = 0.3.

X-ray diffraction (XRD) was also carried out, using a three-circle diffractometer [9], to determine the orientation of both $SrTiO_3$ single crystals and metal thin film samples. The diffractometer was equipped with point-focused Cu radiation ($K\alpha_1$ and $K\alpha_2$), operated at 45 kV and 40 mA, and using an incident beam lens to provide parallel optics. Beam size, divergence, and noise were limited using a 2×2 mm antiscatter slit, a 0.27° Soller slit, and a graphite monochromator. A series of short $2\theta - \theta$ scans were carried out in Bragg–Brentano geometry to determine the bulk substrate and film crystalline orientations. These patterns were each collected at specific values for the angles ϕ and ψ, corresponding to calculated locations of film and substrate (*hkl*) crystal planes. Measurements were carried out using a step size of 0.02° and count time of 0.2 s.

LEED data were obtained from $SrTiO_3$ crystals and Pt films using an electron beam (1 mm diameter, 3 mA current) in a Perkin-Elmer model 15–120 LEED system mounted in an ultra-high vacuum (UHV) chamber. Prior to LEED analysis, the $SrTiO_3$(621) samples were Ar^+ ion sputtered ($P_{Ar} = 10^{-4}$ Torr, 1500 eV gun voltage, 15 mA current) in the UHV chamber while the sample temperature was cycled from −125 to 725 °C at 2 °C/min. After two sputtering cycles, the Ar was evacuated from the

chamber and the same heat treatment was repeated once. After the pre-treatments, the $SrTiO_3$ samples were cooled to −165 °C and placed in front of the LEED optics, where diffraction patterns were recorded at a beam voltage of 220 eV. Such samples did not exhibit any charging problems during LEED experiments.

LEED was carried out on metal films in a manner similar to that used for the bare $SrTiO_3(621)$ substrates. Unfortunately, the Ar^+ ion sputtering treatment used to clean the Cu film surfaces destroyed them prior to LEED analysis. Thus, the surface preparation was modified to avoid de-wetting and carried out on the more robust Pt(621) thin film samples. Surface cleaning was carried out by heating the sample to 315 °C (lower than the annealing temperature for film growth) at 2 °C/min, exposing it to 10^{-4} Torr of O_2 for 10 min, and then cooling (2 °C/min) it to RT. After repeating this O_2 cleaning for 25 cycles, Pt films were then cooled to −175 °C, placed in front of the LEED optics, and patterns were registered under a beam voltage of 250 eV, again with no evidence of charging problems.

3. Results and discussion

3.1. $SrTiO_3(621)$

By locating several known (*hkl*) Bragg XRD peaks, it was confirmed that the $SrTiO_3$ crystals were indeed (621)-oriented in the bulk. AFM surface topographs are given in Fig. 1 for an as-received sample (Fig. 1a) and a thermally treated sample (Fig. 1b). The thermally treated sample was subjected to the most aggressive heating schedule used during the growth of metal films: heating to 600 °C at 15 °C/min, hold at 600 °C for 60 min, and cooling to room temperature at no faster than 20 °C/min. In both topographs, no discernible features are observed and both samples exhibit atomically flat surfaces with root-mean-square (rms) roughness values of ≈1.5 Å. These results imply that the local surface normal is parallel to the global surface normal for both samples, and that the surface is stable against macrofacet formation during heating. The latter result is important because the samples are heated during LEED characterization to clean the surfaces and during thin film deposition to attain epitaxy. It has been observed elsewhere [26] that, at much higher temperatures than those used for surface cleaning in LEED and for thin film deposition, large-scale faceting occurs for all surfaces in the vicinity of the (621) plane. The topograph in Fig. 1b demonstrates the important point that the $SrTiO_3(621)$ surface remains stable under our conditions.

It should be noted that well-ordered, ideal chiral surfaces should exhibit featureless topographs, because the surface microfacets are too closely spaced to be observed with the AFM technique [9]. The ideal surface structure of $SrTiO_3(621)$ is presented in Fig. 2a, where it can be seen clearly that the kinked steps are separated by just a few atomic distances. This is the also the case for the Pt(621) surfaces, whose ideal structure is shown in Fig. 2b. (In both cases, the kinked steps are highlighted to illustrate the naturally chiral nature of the surfaces.) However, poorly-ordered surfaces, such as those which are often observed on low-index $SrTiO_3$ crystals that have been mechano-chemically polished and not subjected to any thermal treatment [15,20], also exhibit featureless topographs. We cannot distinguish between these two cases based on Fig. 1. However, these images do illustrate that the as-received and thermally treated substrates are atomically flat and are suitable for both characterization using LEED and epitaxial thin film growth.

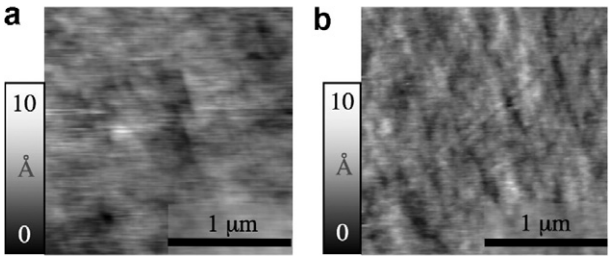

Fig. 1. AFM topographic images of $SrTiO_3(621)$ substrate surfaces that are (a) as-received and (b) annealed at the deposition temperature (600 °C) in 10^{-5} Torr. The grayscale height color key is given on the left of both images.

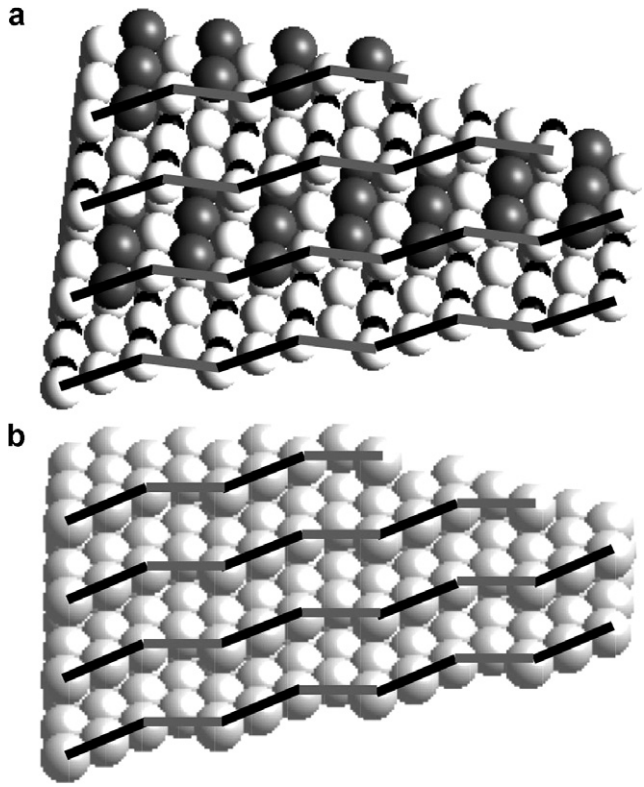

Fig. 2. Views of (a) $SrTiO_3(621)$ and (b) Pt(621) surfaces. Surface steps are indicated by lines denoting directions in the (1 1 1) (black) and (1 1 0) (grey) nanospaced microfacets.

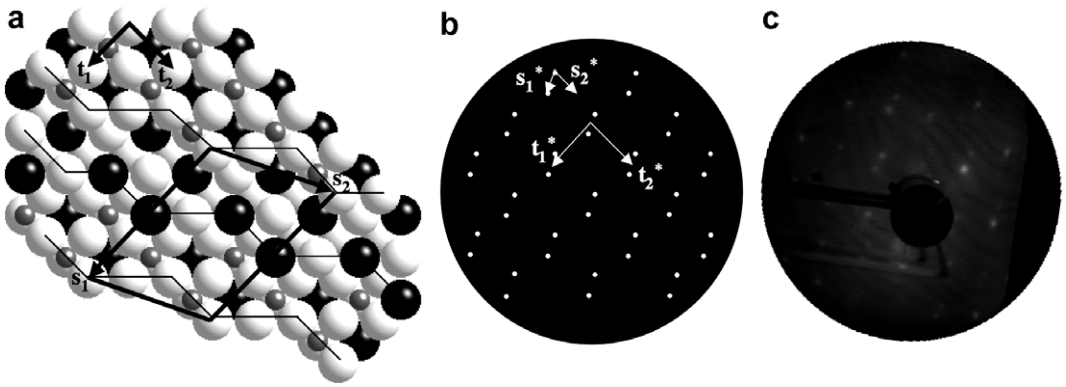

Fig. 3. (a) Ideal crystal structure representation, and (b) theoretical and (c) experimental LEED patterns, of the $SrTiO_3(621)$ surface. In (a), the view direction is along [100], the small gray spheres represent Ti, the large dark spheres represent Sr, and the large light spheres represent O. Thin dark lines denote the kinked step edges along the (100) terraces. The thicker lines outline the surface unit cell. In (a) and (b), the surface (621) unit cells are denoted by $\mathbf{s}_n$ (real) and $\mathbf{s}_n^*$ (reciprocal) vectors; terrace (100) unit cells are marked as $\mathbf{t}_n$ (real) and $\mathbf{t}_n^*$ (reciprocal).

An as-received $SrTiO_3(621)$ sample was then introduced into the LEED chamber to determine if its surface was crystalline and if it exhibited chirality. Fig. 3a is a schematic diagram of an ideal $SrTiO_3(621)$ surface that illustrates the relevant surface crystallographic vectors. The overall surface, whose unit cell is described by $\mathbf{s}_1$ and $\mathbf{s}_2$, is composed of terraces having (100) character (which are described by $\mathbf{t}_1$ and $\mathbf{t}_2$), separated by nanospaced steps running along the $[0\bar{1}2]$ direction ($\mathbf{s}_2$). LEED patterns taken from such surfaces have the basic geometry of the infinite terrace plane, plus splitting of diffracted spots arising from the steps [28–31], as shown in the schematic LEED pattern of Fig. 3b. The pattern shown in Fig. 3b was generated using the framework presented in Refs. [28–31], and as described below.

The expected LEED pattern consists of diffraction spots located around nodes corresponding to the terrace reciprocal lattice ($\mathbf{t}_1^*$ and $\mathbf{t}_2^*$). Diffraction intensity at each node exists inside a so-called "diffraction envelope" (a region of reciprocal space in which diffraction intensity is allowed) having a length and direction determined by the surface reciprocal lattice vector normal to the step edge ($\mathbf{s}_1^*$). Rather than having single spots at the nodes, which would be the case for an infinite terrace, the observed spots can be split along the $\mathbf{s}_1^*$ direction owing to the interference of diffracted beams from terraces at different heights. The basic pattern can be easily constructed by overlaying the diffraction envelope pattern with the diffraction "fringes," or lines which represent the splitting, that are separated by $\mathbf{s}_1^*$ and that run parallel to the other surface reciprocal lattice direction ($\mathbf{s}_2^*$). Diffracted intensity is observed when these fringes intersect the diffraction envelopes around the nodes.

It is important to note, however, that the terrace pattern and the fringes do not share a common origin in reciprocal space; their relative positions are determined by the angle (α) between surface and terrace. Since both the terrace pattern and fringe patterns vary with incident electron energy, the observed overall pattern will be energy-dependent as well. (Regardless of the incident energy, all diffraction spots in a chiral pattern must exist at nodes corresponding to the surface reciprocal lattice, $\mathbf{s}_1^*$ and $\mathbf{s}_2^*$, although not all nodes need to have intensity; only such $\mathbf{s}_n^*$ nodes that exist in the diffraction envelopes around the $\mathbf{t}_n^*$ nodes have intensity.) An ideal pattern can still be easily constructed within this framework by selecting an incident electron energy (and associated λ) such that the distance between terrace and fringe origins (l) is an integer multiple of the spacing between lattice fringes $\left(\frac{\lambda}{|\mathbf{s}_1|\cos\alpha}\right)$. This allows for a uniform splitting of spots in the diffraction pattern. Fig. 3b shows an example of this ideal pattern for the $SrTiO_3(621)$ surface shown in Fig. 3a. This pattern consists of a square arrangement of doublet spots, where the doublet axis ($\mathbf{s}_1^*$) lies at an angle with respect to the reciprocal lattice directions describing the nearly square pattern ($\mathbf{t}_1^*$ and $\mathbf{t}_2^*$).

The experimental LEED pattern registered from the $SrTiO_3(621)$ surface is shown in Fig. 3c. The observed pattern is in good agreement with the expected pattern shown in Fig. 3b, which was generated for the ideal diffraction conditions of an ideal surface. The experimental LEED pattern indeed lies on a (100)-type grid, with diffracted doublets occurring around each node in the (100)-type grid, and the direction and magnitude of the spot splitting correspond roughly to those expected from the surface reciprocal lattice vector $\mathbf{s}_1^*$. This LEED pattern demonstrates that naturally chiral ceramic surfaces can be prepared by cleaving along high-index crystal directions in a manner analogous to fcc metals. The observation that some of the diffraction doublets in the experimental pattern do not have identical and symmetric intensities can be simply ascribed to the fact that the diffraction conditions have not been optimized with respect to the ideal case described above. All observed diffractions spots in the experimental pattern do indeed exist at nodes corresponding to the surface reciprocal lattice ($\mathbf{s}_1^*$ and $\mathbf{s}_2^*$) of $SrTiO_3(621)$, again attesting to the chiral nature of this surface. Importantly, the net surface chirality implies that this substrate can drive the enantiospecific heteroepitaxial growth of chiral fcc(621) films, as has been previously observed for Pt [9]. It also

implies that naturally chiral ceramic surfaces can exhibit enantioselective properties. It should be noted that we have not explored the chemical nature of the surface; we have only explored the crystal symmetry of the surface, which is consistent with the expected symmetry from an ideal $SrTiO_3$(621) plane. In the above experiments, we used a sputtering treatment to clean the as-received surfaces; in the following section, we present the results of heteroepitaxial thin film growth experiments that indicate that similar chiral surfaces are produced through more mild surface cleaning procedures and that these surfaces can drive enantioselective processes.

3.2. Pt and Cu films

The deposition of epitaxial Pt(621) films has been discussed at length in the previous work [9]; analogous results are presented here for growth of Cu(621) samples on $SrTiO_3$(621) single crystals. The XRD pattern in Fig. 4 is a composite of several short scans taken from different regions in diffraction space on a Cu/$SrTiO_3$(621) sample. In each case, a given (*hkl*) peak from the $SrTiO_3$ substrate is located by calculating its position relative to the global surface normal of (621) and by rotating the diffractometer around the surface normal (by an angle ϕ) and around an axis in the substrate plane, perpendicular to the surface normal (by an angle ψ) to locate that reflection. The presence of a Cu peak of the same (*hkl*) at the same angles of ϕ and ψ (but at a different 2θ value, since the materials have different lattice parameters and the Cu films are fully relaxed) demonstrates that a Cu film with the same orientation as the $SrTiO_3$ crystal is present. The Cu peaks are all located at the 2θ positions calculated for bulk Cu, which indicates that the films are fully relaxed (as observed for Cu(100) films on $SrTiO_3$(100) [19]). Several such scans, along with the absence of other Cu diffracted intensity elsewhere, prove that epitaxial Cu(621) films can be deposited. This result is exactly analogous to the situation for Pt(621); XRD conclusively demonstrates that both metals can be deposited epitaxially on $SrTiO_3$(621) substrates using the three step process.

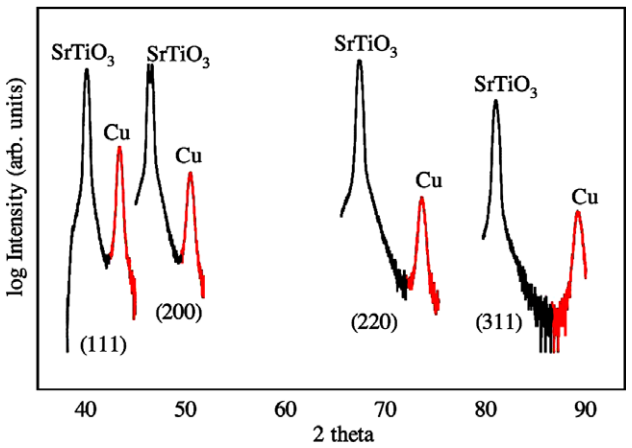

Fig. 4. Composite XRD pattern for a Cu(621) film grown on $SrTiO_3$(621). It should be noted that each of the diffraction doublets were collected at different angles of ϕ and ψ: the ψ-values were, respectively for the (111), (200), (220), and (311) reflections, 35.75°, 20.44°, 27.94°, and 8.56°. The ϕ-values depend on the arbitrary mounting of the crystal on the goniometer, but all values were self-consistent.

The surface morphologies that developed during the three-step process for both Cu and Pt films are given in Fig. 5. The Cu film surface (Fig. 5a) is nearly perfectly flat, with rms roughness of just 3 Å and no visible surface features. The flat surface morphology of the Cu film along with its (621) orientation makes it a prime candidate to display a chiral surface. Pt films were also found to have surfaces characterized by large flat areas separated by small pinholes (Fig. 5b), with an overall rms roughness of 9 Å. Pinholes develop during the annealing stage of film formation (step three), which is carried out at 600 °C. Because Pt does not prefer to wet the $SrTiO_3$ surface, the pinholes likely form as a de-wetting mechanism [32–34]. In this work, we are concerned with the crystallographic nature of the large flat areas between pinholes; these regions represent the epitaxial crystal surface. Copper films, on the other hand, were found to be pinhole free when using the three step deposition conditions described above. For both films, the combination of XRD and AFM results suggests net chirality at the film surface, but surface science techniques are necessary to verify this inference.

LEED experiments were performed to probe the surface crystallography of the metal thin films. Patterns were recorded from the Pt(621) sample, because the Cu films were lost in a sputtering process intended to clean the surface. Fig. 6a gives a schematic representation of an ideal Pt(621) surface, and Fig. 6b gives a theoretical diffraction pattern constructed in the same manner as was done for the pattern illustrated in Fig. 3b. Although the unit cells of the terrace ($\mathbf{t}_1$ and $\mathbf{t}_2$) and surface ($\mathbf{s}_1$ and $\mathbf{s}_2$) of Pt are similar to those of $SrTiO_3$(621), owing to their structural similarities, both sets of vectors are shorter for Pt owing to its simpler surface composition. The calculated pattern given in Fig. 6b again illustrates the features characteristic of a chiral surface: a basic square pattern given by the terrace reciprocal lattice vectors ($\mathbf{t}_1^*$ and $\mathbf{t}_2^*$) with splitting of diffracted spots along a direction normal to the step edge ($\mathbf{s}_1^*$).

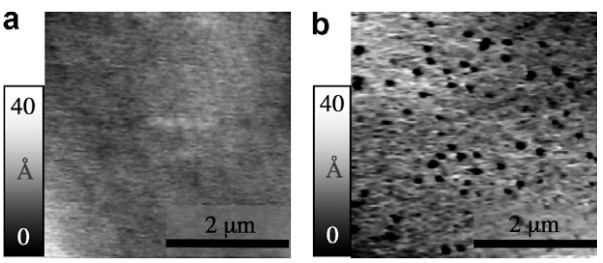

Fig. 5. AFM topographic images of (a) Cu(621) and (b) Pt(621) films. The rms roughness values are (a) 3 and (b) 9 Å. The grayscale height key is given on the left of both images.

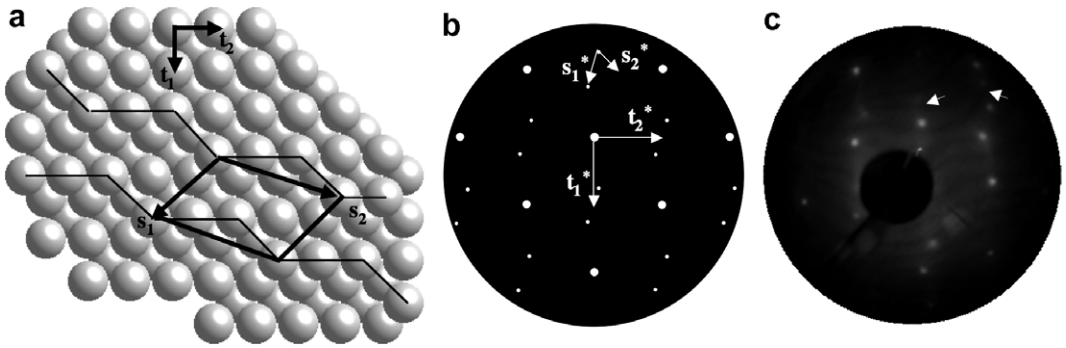

Fig. 6. (a) Ideal crystal structure representation, and (b) theoretical and (c) experimental LEED patterns of the Pt(621) surface. In (a), the view direction is along [1 0 0]. Thin dark lines denote the kinked step edges along the (1 0 0) terraces. The thicker lines outline the surface unit cell. In (a) and (b), surface (621) unit cells are denoted by $\mathbf{s}_n$ (real) and $\mathbf{s}_n^*$ (reciprocal) vectors; terrace (1 0 0) unit cells are marked as $\mathbf{t}_n$ (real) and $\mathbf{t}_n^*$ (reciprocal).

While the ideal Pt(621) LEED pattern in Fig. 6b is qualitatively very similar to the $SrTiO_3$(621) pattern given in Fig. 3b, there are a few intrinsic differences. For the ceramic $SrTiO_3$(621) surface, each node on the LEED pattern contained a diffracted doublet; because of additional symmetry elements on the Pt(621) surface, nodes along both $\mathbf{t}_1^*$ and $\mathbf{t}_2^*$ alternate between single spots and diffracted doublets for Pt (note that this is for the ideal case where the origin of the fringes and the terrace reciprocal lattice coincide). Also, the reciprocal space spots are more widely split in the Pt pattern because the real steps are more closely spaced; compare the lengths of $\mathbf{s_1}$ for the two surfaces. As described earlier, the theoretical pattern shown in Fig. 6b is expected only for a particular electron λ for which the terrace and fringe diffraction patterns are coincident. Using other incident electron energies for LEED will cause the fringes to intersect the diffraction envelopes at different positions, causing the observed pattern to differ from that predicted for a specific electron wavelength. The LEED pattern for an arbitrary electron energy will have doublets at each node with highly asymmetric intensity ratios between the two peaks. Again, all spots corresponding to the (621) pattern will exist at the nodes of a lattice based on the vectors $\mathbf{s}_1^*$ and $\mathbf{s}_2^*$.

The experimental LEED pattern of a Pt film is given in Fig. 6c and it is in reasonable agreement with the predicted patterns, demonstrating that the chiral $SrTiO_3$(621) surface can drive growth of homochiral surfaces on Pt(621) thin films. It does appear, however, that diffracted spots are split in a less uniform manner for Pt(621) than for $SrTiO_3$(621), implying that the electron energy does not correspond to the ideal case. During our experiments, the electron energy was adjusted during collection with the goal of producing sharp spots; the asymmetric and non-uniform spot splitting in our experimental Pt LEED pattern is likely a result of this arbitrary selection of the incident electron energy, although thermal roughenning of the steps cannot be ruled out either. As described above, all spots should exist at nodes of a grid built up from the vectors $\mathbf{s}_1^*$ and $\mathbf{s}_2^*$. In fact, all spots but the two weak peaks marked with arrows do indeed fall on such a grid, indicating that the surface is a chiral, crystalline Pt(621) surface. The important result here is that a chiral ceramic surface has been used to drive the growth of a thin metal film having a single homochiral surface orientation. Given that the Cu films also displayed bulk film crystallinity and surface morphologies superior to the Pt films, it can be surmised that the Cu films also exposed chiral surfaces.

Recently, Monte Carlo simulations were used to describe the microstructural evolution during the post-deposition annealing stage of chiral Pt film growth [21]. In Fig. 7 we present images of three relevant microstructures (adapted from Ref. [21]) to discuss the existence of the two extra spots that appear in the LEED patterns for Pt(621) films. Fig. 7a represents a cross-sectional view of the initial state of the film prior to annealing (see caption and Ref. [21] for details). During annealing all grains grow but the epitaxial seeds coalesce and ultimately consume the matrix grains, resulting in a chirally-oriented film with a pure chiral surface (Fig. 7c). If, however, the annealing is terminated just prior to completion, a few large grains

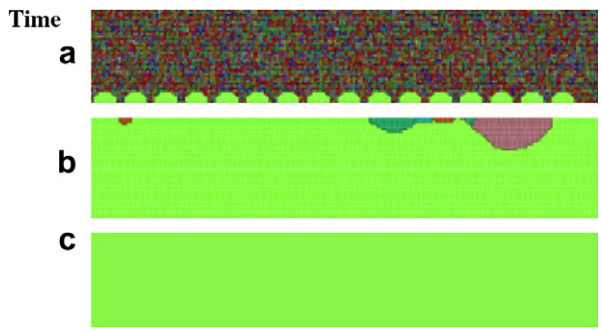

Fig. 7. Cross-sectional microstructural slices from 3-D Monte Carlo simulations of epitaxial grain growth in Pt films formed using the three step process (see Ref. [21] for details). (a) The pre-annealed state in which the epitaxial seed grains are light gray in color and reside at the bottom of the image while the polycrystalline matrix consists of randomly-oriented grains that are represented by variations in grayscale in the upper portion of the film.The different grayscales indicate regions of the film having different orientations. (b) A nearly completely converted film, having a few surface grains of alternate orientations. (c) A completely converted epitaxial film with a pure chiral surface.

remain at the surface as shown in Fig. 7b (not given in Ref. [21]). The coexistence in the LEED pattern (given in Fig. 6c) of spots arising from the chiral surface and two weak spots that do not lie at nodes of the chiral surface lattice indicate that this particular film corresponds to a final state like that given in Fig. 7b, having a few persistent non-epitaxial grains at the surface. However, the major portion of the surface is indeed chiral and has the same orientation as the underlying ceramic substrate. Additional annealing would remove these few remaining surface grains [21].

In summary, we have demonstrated that Pt(621) thin films having chiral surfaces can be deposited heteroepitaxially on naturally chiral $SrTiO_3$(621) ceramic substrates. Both $SrTiO_3$ single crystals and Pt films were verified to have a bulk (621) orientation and to be atomically flat by XRD and AFM experiments, and their surfaces were shown to be homochiral by splitting of diffracted spots in LEED patterns. These results show that thin film processing can be used to obtain chiral metal surfaces and offer promise for the development of large-area surfaces for enantiospecific or enantioselective applications.

Acknowledgements

A.J.F. was supported by a National Defense Science and Engineering Graduate fellowship sponsored by the Office of the Deputy Under Secretary of Defense for Science and Technology and the Army Research Office. This work was also supported partially by the MRSEC program of the National Science Foundation under Award Number DMR-0079996.

References

[1] C.F. McFadden, P.S. Cremer, A.J. Gellman, Langmuir 12 (1996) 2483.
[2] R.M. Hazen, D.S. Sholl, Nat. Mater. 2 (2003) 367.
[3] D.S. Sholl, A. Asthagiri, T.D. Power, J. Phys. Chem. B 105 (2001) 4771.
[4] G.A. Attard, J. Phys. Chem. B 105 (2001) A.
[5] J.D. Horvath, A.J. Gellman, J. Am. Chem. Soc. 123 (2001) 7953.
[6] A. Ahmadi, G. Attard, J. Feliu, A. Rodes, Langmuir 15 (1999) 2420.
[7] G.A. Attard, A. Ahmadi, J. Feliu, A. Rodes, E. Herrero, S. Blais, G. Jerkiewicz, J. Phys. Chem. B 103 (1999) 1381.
[8] J.D. Horvath, A.J. Gellman, D.S. Sholl, T.D. Power, in: Physical Chemistry, Oxford University Press, Washington, DC, 2002, p. 269.
[9] A.J. Francis, P.A. Salvador, J. Appl. Phys 96 (2004) 2482.
[10] G.S. Rohrer, Structure and Bonding in Crystalline Materials, Cambridge University Press, Cambridge, 2001.
[11] A.J. Francis, P.A. Salvador, J. Mater. Res. 22 (2007) 89.
[12] B.S. Kwak, P.N. First, A. Erbil, B.J. Wilkens, J.D. Budai, M.F. Chisholm, L.A. Boatner, J. Appl. Phys. 72 (1992) 3735.
[13] A.D. Polli, T. Wagner, T. Gemming, M. Rühle, Surf. Sci. 448 (2000) 279.
[14] T. Wagner, A.D. Polli, G. Richter, H. Stanzick, Z. Metallkd. 92 (2001) 701.
[15] A. Asthagiri, C. Niederberger, A.J. Francis, L.M. Porter, P.A. Salvador, D.S. Sholl, Surf. Sci. 537 (2003) 134.
[16] G.R. Harp, R.F.C. Farrow, R.F. Marks, J.E. Vazquez, J. Cryst. Growth 127 (1993) 627.
[17] X. Chen, T. Garrent, S.W. Liu, Y. Lin, Q.Y. Zhang, C. Dong, C.L. Chen, Surf. Sci. 542 (2003) L655.
[18] K. Zhao, H.K. Wong, J. Cryst. Growth 256 (2003) 283.
[19] A.J. Francis, Y. Cao, P.A. Salvador, Thin Solid Films 496 (2006) 317.
[20] A.J. Francis, P.A. Salvador, in: 106th Annual Meeting and Exposition of the American Ceramic Society, Indianapolis, U.S.A., Ceramic Transactions 158 (April 2004) 37.
[21] A.J. Francis, C.G. Roberts, Y. Cao, A.D. Rollett, P.A. Salvador, Acta Met., in review.
[22] T.-D. Doan, J.L. Giocondi, G.S. Rohrer, P.A. Salvador, J. Cryst. Growth 225 (2001) 178.
[23] N. Erdman, K.R. Poeppelmeier, M. Asta, O. Warschkow, D.E. Ellis, L.D. Marks, Nature 419 (2002) 55.
[24] M. Kawasaki, K. Takahashi, T. Maeda, R. Tsuchiya, M. Shinohara, O. Ishiyama, T. Yonezawa, M. Yoshimoto, H. Koinuma, Science 266 (1994) 1540.
[25] T. Nishimura, A. Ikeda, H. Namba, T. Morishita, S. Kido, Surf. Sci. 421 (1999) 273.
[26] T. Sano, D.M. Saylor, G.S. Rohrer, J. Am. Ceram. Soc. 86 (2003) 1933.
[27] T. Wagner, G. Richter, M. Rühle, J. Appl. Phys. 89 (2001) 2606.
[28] J. Perdereau, G.E. Rhead, Surf. Sci. 24 (1971) 555.
[29] G.E. Rhead, J. Perdereau, C.R. Acad. Sci. Paris 269 (1969) 1183.
[30] G.E. Rhead, J. Perdereau, C.R. Acad. Sci. Paris 269 (1969) 1261.
[31] G.E. Rhead, J. Perdereau, C.R. Acad. Sci. Paris 269 (1969) 1425.
[32] S. Roberts, R.J. Gorte, J. Phys. Chem. 95 (1991) 5600.
[33] L. Ruan, D.M. Chen, Appl. Phys. Lett. 72 (1998) 3464.
[34] R.T. Tung, J.L. Batstone, Appl. Phys. Lett. 52 (1988) 648.